Grain-size effects on the deformation in nanocrystalline multi-principal element alloy

Article *in* Materials Chemistry and Physics · December 2021

DOI: 10.1016/j.matchemphys.2021.125546

Grain-size effects on the deformation in nanocrystalline multi-principal element alloy

Ankit Roy[a], Ram Devanathan[b], Duane D. Johnson[c,d] and Ganesh Balasubramanian[a, r]

[a]*Department of Mechanical Engineering and Mechanics, Lehigh University, Bethlehem, PA*

[b]*Pacific Northwest National Laboratory, Richland, WA 99354, USA*

[c]*Department of Materials Science and Engineering, Iowa State University, Ames, IA 50011*

[d]*Ames Laboratory, United States Department of Energy, Iowa State University, Ames, IA 50011, USA*

Abstract

Multi-principal element alloys (MPEAs) continue to garner great interest due to their potentially remarkable mechanical properties, especially at elevated temperatures for key structural and energy applications. Despite extensive literature examining material properties of MPEAs at various compositions, much less is reported about the role of grain size on the mechanical properties. Here, we examine a representative nanocrystalline BCC refractory MPEA and identify a crossover from a Hall-Petch to inverse-Hall-Petch relation. While the considered MPEA predominantly assumes a single-phase BCC lattice, the presence of grain boundaries imparts amorphous phase distributions that increase with decreasing grain size (i.e., increasing grain boundary volume fraction). Using molecular dynamics simulations, we find that the average flow stress of the MPEA increases with decreasing average grain size, but below a critical grain size of 23.2 nm the average flow stress decreases. This change in the deformation behavior is driven by the transition from dislocation slip to grain-boundary slip as the predominant mechanism. The crossover to inverse-Hall-Petch regime is correlated to dislocation stacking at the grain boundary when dislocation density reaches a maximum.

KEYWORDS: *multi-principal element alloys, nanocrystalline grains, molecular dynamics, Hall-Petch relation, dislocation slip.*

[r] Corresponding author. Email: bganesh@lehigh.edu. Phone: +1-610-758-3784.
Address: Packard Laboratory 561, 19 Memorial Drive West, Bethlehem, PA 18015, USA

1. Introduction

Multi-principal element alloys (MPEAs) [1, 2] have disrupted metallurgical research with an exponential surge in the related literature over the last decade [3]. In essence, the concept of high-entropy alloys (HEAs), a subset of MPEAs, is grounded in the thermodynamic principle that a high configurational entropy can lower the Gibbs free energy and promote a stable single-phase crystallographic structure [2, 4-6]. Currently various models exist that predict the phase and mechanical properties of different MPEA compositions guided by materials chemistry [7, 8]. Some of these approaches employ thermodynamic [9], crystallographic [10] and electronic descriptors [11] to predict the alloy phases, while more recent efforts feed multiple alloy features into a machine-learning framework to estimate the crystal structure and mechanical properties, such as hardness [12] and Young's modulus [13]. Also, density-functional-theory (DFT) based methods incorporating thermodynamics (i.e., configurational averaging and short-range order) have been quantitatively successful, [14-16] even identifying electronic origins for properties [17, 18]. Regardless, it is evident from the literature that the microstructure, grain size and chemical composition of MPEAs play a crucial role in determining their mechanical properties [19-22]. Examining the effect of grain size variations facilitate our understanding of the deformation mechanism during plastic flow, in addition to them directly impacting the alloy strength.

Hall [23] and Petch [24] first demonstrated the effect of reducing the grain size on structural properties via the relation $\sigma_y = \sigma_0 + k_y d^{-1/2}$, where σ_y is the yield stress, d is average grain diameter, and σ_0 and k_y are materials-specific constants. They proposed that grain boundaries (GB) result in discontinuity of slip planes and hinder transmission of dislocations from one grain to another [25]. Hence, as grains become smaller, the effect of dislocation obstruction increases thereby increasing the strength of the material; however, as the grain size approaches nanoscale, this effect reverses [26]. For nanocrystalline materials, the role of GBs becomes more pronounced as the volume fraction occupied by GBs is comparable to that of the bulk crystal. Below a critical grain size, the material begins to soften [27] limiting the maximum strengthening achievable by the Hall-Petch phenomenon. The dominant deformation mechanism changes from intragranular to intergranular as the volume fraction of GBs increase [28].

The origins of GB strengthening, work-hardening and plastic deformation are rooted in atomic-scale mechanisms [27, 29, 30]. Prior literature [31] employing molecular dynamics (MD) simulations to examine the role of decreasing grain size on the deformation behavior of nanocrystalline BCC Fe concluded that the primary mechanism changes from dislocation sliding to GB rolling and sliding below a grain size of 19.7 nm, *i.e.*, the transition to the inverse Hall-Petch phenomenon. Likewise, Schiøtz et al. [27] probed nanocrystalline copper and eliminated the influence of diffusion on the deformation characteristics at room temperature, in contrast to a previous report [26]. Recently, Jones et al. [32] demonstrated that in an ultra-high vacuum environment, a single-phase CoCrFeMnNi HEA exhibits low-friction and high-wear resistance. This behavior was attributed to the extreme grain refinement under a high-shear rate, resulting in near amorphization on the surface layer that generates the wear particles, indicating an occurrence of inverse Hall-Petch phenomenon. Note that, in the absence of oxides, the coefficient of friction for metals represents a metric for surface shear strength that could be correlated to the grain size at the surface of contact [23, 24].

Given the limited literature on the Hall-Petch strengthening of MPEAs, such as $CoNiFeAl_xCu_{(1-x)}$ [33], we employ molecular dynamics (MD) simulations to scrutinize the effect of grain size on the strengthening and deformation mechanism in a representative MPEA. In particular, we consider a certain composition of refractory Mo-W-Ta-Ti-Zr MPEA that was reported to exhibit 3× higher Young's modulus (~340 GPa at room temperature) than the equiatomic HEA counterpart [30]. This alloy $(Mo_{0.95}W_{0.05})_{0.85}Ta_{0.10}(TiZr)_{0.05}$ predicted to possess a higher Young's modulus (~2× at 2000 K) relative to commercial alloys (such as TZM) is used as the testbed for our grain-size simulations. As discussed in the methods section, the flow stress of this nanocrystalline BCC MPEA increases with decreasing average grain size (Hall-Petch relation); however, below a critical grain size of ~23.2 nm the flow stress decreases because of the transition from dislocation slip to grain boundary slip as the driving deformation mechanism.

2. Computer simulation methods

Classical MD simulations are performed using the extensively parallelized Large-scale Atomic/Molecular Massively Parallel Simulator (LAMMPS) package [34], while OVITO [35] is

used for visualization and data-processing. Four (4) cubic simulation cells containing 5 grains each and one (1) cubic cell containing 2 grains in random orientations are constructed using the Voronoi tessellation method incorporated in the ATOMSK toolkit [36]. First a unit cell for the MPEA composition is generated with BCC crystal structure. Then a fixed number of nodes are introduced at random positions inside the simulation box. These nodes serve as centers for each of the grains. Subsequently, grains positioned at those nodal points but with random orientations are constructed using the Voronoi tessellation algorithm within the simulation box. The edge lengths of the 4 samples with 5 grains each are 5 nm, 20 nm, 30 nm and 40 nm, while the edge of the simulation cell containing 2 grains is 40 nm long. Notably, a 40 nm cell accommodates more than 4 million atoms. We limit the box size to 40 nm edge lengths because generation of simulation boxes > 40 nm edge length proved to be computationally expensive. The mean grain sizes in the 5 simulated samples are 3.1 nm, 11.7 nm, 17.5 nm, 23.2 nm, 31.7 nm, respectively. The grain orientation in each simulation box is randomized so as to best replicate an experimental scenario wherein each synthesized sample would have a random orientation of grains and typically different from all other samples. Such a methodology has been adopted in the literature [31, 37] simulating the inverse Hall-Petch phenomenon.

For comparison, the range of grain sizes chosen in this work has been set slightly larger than the range adopted in (i) Ref. [31] where the inverse Hall-Petch behavior was studied in cubic iron and the grain sizes were varied from 3.7 nm to 19.7 nm with 14.7 nm emerging as the critical grain size, (ii) Ref. [33] where CoNiFeAlCu alloy grains were varied from 7.2 to 23.4 nm and the critical grain size was noted to be 18.9 nm. Other works analyzing the Hall-Petch to inverse Hall-Petch transition have used similar range of grain sizes. This is done so as to encompass a wider range of grain sizes and understand how the critical grain size changes depending upon the nature of elements used in alloying.

The interatomic interactions are described by EAM (embedded-atom potentials) [38]. The EAM potential is a multibody potential which is expressed as $E = F_\alpha \sum_{j \neq i} \rho_i\left(R_{i,j}\right) + \frac{1}{2}\sum_{j \neq i} \emptyset_{\alpha,\beta}(R_{i,j})$, where E is the total energy of the atomistic system obtained by the summation of embedding energy F on the i^{th} atom and the short range pair potential energy $\emptyset$, α and β being the element types of atoms i and j, $R_{i,j}$ being the distance between i^{th} and j^{th} atoms and ρ being the electron

density. This potential has been previously used and validated for mechanical properties of this MPEA by comparing to DFT-derived values [30] and for obtaining the diffusion coefficients in $(Mo_{0.95}W_{0.05})_{0.85}Ta_{0.10}(TiZr)_{0.05}$ [22]. We utilize the parameter combinatorial tool available in the LAMMPS package [38] to construct a forcefield that includes all 10 cross interactions between the elements in the Mo-Ta-Ti-W-Zr MPEA. This technique was adopted previously to simulate crystallographic phase and stress-strain behavior for $Al_{10}CrCoFeNi$ [39, 40] and $(Mo_{0.95}W_{0.05})_{0.85}Ta_{0.10}(TiZr)_{0.05}$ [22, 30]. In addition, the BCC phase and modulus of elasticity of the Mo-Ta-Ti-W-Zr MPEA obtained from MD simulations corroborate with experimental results[22]. We validate the potential by using the equiatomic MoTaTiWZr alloy as a testbed. We show that the equiatomic composition forms a predominantly BCC phase as depicted in Fig. 1. The equiatomic composition has been shown to form a purely BCC phase experimentally in a prior work [30]. Thus, we establish that the potential adopted in this work is able to yield results with reliable accuracy. Recent works have used machine-learning to develop moment tensor potentials (MTPs) [41] for various bcc refractory alloys, such as MoNbTaVW, MoNbTaW and MoNbTa, and have shown them to be appreciable accurate. The predicted values of free energy for the above mentioned alloys using these potentials are within 2 meV/atom of DFT values which is more accurate than EAM by an order of magnitude [42]. But these potentials have not been developed for the alloy system under consideration here and hence we continue to use the EAM potentials that have been successfully used in notable prior works, as mentioned earlier. Moreover the analysis of deformation mechanisms in metals and alloys using MD has been mostly carried out with EAM potentials in most previous works [31, 33, 37], justifying the use of existing EAM potentials for Mo-Ta-Ti-W-Zr in this work.

The lattice was energy minimized using the conjugate-gradient method with an energy tolerance in LAMMPS of 10^{-15} eV and a force tolerance of 10^{-15} eV/Å. The alloy simulation was initialized at 1300 K under an isothermal-isobaric (NPT) ensemble for 50 ps at 0 MPa and then rapidly quenched to 300 K in 500 ps. This initialization temperature was considered to prevent complete melting of the alloy to liquid state, lest a single crystal may result upon quenching from a higher temperature and the GBs incorporated prior to quenching might be lost or re-oriented. Similar temperature limits for quenching HEAs with GBs was discussed previously [43]. Periodic boundary conditions are applied in all the directions [31]. The quenched alloy was further

equilibrated under NPT and NVE ensembles for 90 ps each thereby completing the quenching process. Quasi-static unidirectional tensile deformation was executed at a strain rate of 0.01 ps^{-1} along the x-direction. The strain rate adopted here was previously employed for analyzing the dislocation dynamics of AlCoCrFeNi HEA [29] and Mo-Ta-Ti-W-Zr [14]. We note that the simulated strain rate is several orders of magnitude higher relative to experiments, necessitated by the timescales feasible in MD simulations [44]. However, such simulation procedures do not influence the physical insights derived on the deformation mechanisms as our objective is to investigate the transition in deformation mechanism from larger to smaller grains at an identical strain rate for all the simulated cases. These deformation characteristics observed in these simulations are representative of those observed in experimentally applied high strain rates [39].

3. Results and discussion

The phases and GBs are visualized throughout the deformation process using *common neighbor analysis* (CNA) [45]. A representative equilibrated simulation cell is illustrated in Fig. 2 (a). The CNA (Fig. 2 (b)) indicates that the MPEA is predominantly a single-phase solid solution with 96.5% BCC structure and ~3.5% amorphous phase constituted by the GBs [26]. The local structural coordination of all the simulated samples, containing 31.7 nm, 23.2 nm, 17.5 nm, 11.7 nm and 3.1 nm grains, respectively, are reproduced in Figs. 2 (b-f), while Fig. 2 (g) presents the fractions of the amorphous and crystalline phases as a function of the grain size. As the grain size is reduced from 31.7 nm to 3.1 nm, the fraction of atoms in GBs increases from 3.5% to 65%, in accord with an earlier report [46]. This observation is attributed to the long-range order that exists within the grains and imparts crystallinity, but the interface between adjacent grains is devoid of order and hence amorphous. The absence of crystallinity in GBs is as predicted by Keblinski et al. [47], where energy distribution functions revealed that GB atoms possess an excess energy with 0.20 eV/atom relative to 0.185 eV/atom of the bulk atoms. This excess energy in GB atoms arises by virtue of intergranular misalignment and inhibits long-range order. Additionally, the CNA results evince that GB regions are indeed amorphous. A series of other recent works have reported similar findings in the GB region. Song et al. [48] found that reducing the grain size in nanopolycrystal Cu, and increasing the amorphous phase boundary improved the plasticity of the material. In their MD simulations, the non structured region was referred to as the amorphous GB region. In another work, Zhao et al. [49] studied TiAl alloy and its creep properties using MD

simulations and found that at a given temperature, the creep phenomenon is dominated by dislocation motions under high stresses while at low stresses it is dominated by the diffusion phenomenon. They used a similar technique as that used in the present work to create GB and categorized the uncoordinated atoms as the GB atoms. Other recent works [50, 51] have similarly classified the uncoordinated atoms as the GB region and hence a similar approach has been adopted in the present work. We delve deeper into understanding the composition of the grain boundaries and with this objective we use the structure file of the simulation box with the 11.7 nm grains to filter out only those atoms that comprise the GB as shown in Fig. 2(h). All other atoms within the grains have been deleted in this visualization. Using this data, we plot the atomic % of each element in the GB and compare it with the ideal atomic % of elements that were prescribed by the theoretical composition of the alloy as shown in Fig. 2 (i). According to our simulations, the concentration of Mo in the GB region is almost identical to the grains, whereas Ta is higher and W is lower in concentration. There is almost no Ti in the GB while Zr is slightly more than the concentration prescribed by the formula. The absence of experimental measurements to validate this concentration distribution is acknowledged. Although our main objective is to understand that the GB region is non crystalline and plays a major role in the reversal of the Hall-Petch phenomenon.

To examine the Hall-Petch and its inverse phenomena, tensile deformation simulations are performed on the MPEA cells. The stress-strain curves for all grain sizes are presented in Fig. 3(a). To quantify the effect of grain size on the deformation behavior of nanocrystalline materials, it is physically more sensible to compare the average flow stress over a fixed range of strain [27, 31, 52] due to a highly amplified strain rate effect on the peak stress. Average flow stress in the range 0 – 15% are therefore considered in this work to reproduce the full range of stresses, after which the stress almost saturates to a constant value. As noted from Fig 3(b), the flow stress is 8.8 GPa for the simulation cell with 31.7 nm grains, but it increases to 9.76 GPa when the grain size reduces to 23.2 nm. With further decrease in grain size, the flow stress drops consistently to 6.53 GPa for 3.1 nm grain size. The inverse Hall-Petch equation is obtained by correlating the flow stress with the average grain size, d, for grains of sizes 23.3 nm and below as in Fig. 3(c). We obtain $\sigma_{flow} = 10.097 - 6.678\, d^{-1/2}$, where the negative slope is indicative of the inverse Hall-Petch effect. Thus,

we predict the critical grain size to be in the neighborhood of ~23.2 nm that initiates the crossover from Hall-Petch to the inverse Hall-Petch regime in $(Mo_{0.95}W_{0.05})_{0.85}Ta_{0.10}(TiZr)_{0.05}$ MPEA.

Such a phenomenon has previously been reported for pure metals, *e.g.*, Cu [27, 53], Pd [26], Ta [37], Fe [31], and also in a MPEA, *i.e.*, $CoNiFeAl_xCu_{(1-x)}$ [33]. Computer simulation on nanocrystalline Cu and the Hall-Petch transition [27] noted the occurrence of a large number of micro-sliding events at the GBs. It was suggested that, as the grain size is reduced, the volume fraction of GBs increased promoting the sliding of GB atoms. Likewise, for BCC Fe [31], for grain sizes < 14.7 nm, a transition to inverse Hall-Petch was noted. The phenomenon was attributed to a decrease in strain accumulation due to smaller dislocation pile-up distances that increased the flow stress required for deformation. On further reducing the grain size below the critical dimension, GB slipping was activated due to the increased volume fraction of GBs that causes plastic deformation at a relatively lower loading. For nanocrystalline Ta [37] an inverse Hall-Petch regime is noted to exist for the grain-size range of 3.5-13 nm. Therein, GB rotation and sliding were identified as the dominant deformation mechanisms in this regime, although certain deformation twins and local phase transformations to FCC and HCP were also reported. More recently, Chen et al. [33] examined $CoNiFeAl_xCu_{(1-x)}$ and concluded that as the grain size is reduced below 12.1 nm the deformation mechanism changes from dislocation slip and deformation twinning to GB rotation and migration.

Next, we scrutinize the microstructural evolution of the 40 nm simulation cell containing 23.2 nm grains relative to that of 5 nm simulation cell with 3.1 nm grains to understand the differences in the deformation mechanism underlying this transition to inverse Hall-Petch behavior. For the smaller grain size of 3.1 nm, the predominant deformation mechanism is due to the migration of GBs. The deformation at various stages of straining are reproduced in Fig. 4. The progressive thickening (by ~60%) and alterations in the GB orientations indicate the sliding of GB atoms over each other generating a micro-sliding mechanism. The structural transformation of GB can be characterized by a shear stress $\tau_s^{(i)}$ that denotes the resistance to free sliding (i being the grain misorientation relative to the GB plane) over a planar GB [54]. GBs have a faceted structure where planar regions of GB atoms are bound by kinks and edges, such that GB microsliding is initiated over a GB facet when the applied shear stress exceeds $\tau_s^{(i)}$. The GB microsliding reduces the flow

stress that is otherwise required for straining the crystalline bulk material, as discussed previously for metals [27] and alloys [33]. A deeper probe into the grains highlighted as S and R in Figs. 4(a) and (c) indicates that the dislocation in grain S percolates into the GB and emerges through the other side. This percolation and propagation of a dislocation through GB has been conjectured as the cause for Hall-Petch breakdown [55].

Further straining causes the GBs to thicken to ~8–9 atomic layers due to microsliding [54] as displayed in Figs. 4(d) and (e), and primarily facilitates the deformation in the nanocrystalline grains. While probing the deformation mechanism in the 40-nm-simulation cell with 23.2 nm grains, we find a strong manifestation of FCC phases forming locally, as illustrated in Figs. 4 (f), (g) and (h). The BCC to FCC stress induced transformation has been previously described to be a dominant deformation mechanism in BCC materials [33]. Prior work [56] has reported that the FCC phases nucleate in BCC matrix during the deformation of Pd-Cu alloys via the slip of edge dislocation $a_{bcc}[1\ 1\ 1]/6$ on (0 1 1) BCC slip planes and form a standard FCC matrix by undergoing an expansion in the crystal volume. Such stress-induced phase transformations were also described during the deformation of BCC Ta and the newly formed FCC phase was found to increase in its volume fraction till a peak before saturating to a constant value [37]. An inspection of our results in Figs. 4(f), (g) and (h) reveal an increase in the FCC phase volume fraction from 1.2% to 4.3%, consistent with the trends reported in literature [37].

To reason quantitatively the observed trends in flow stress as a function of grain size, we consider a more robust relationship established between the flow stress and dislocation density. The dislocation evolution of ½<111>-type dislocations for all simulation boxes at a consistent strain level is shown qualitatively in Fig. 5 for various grain sizes at 5% strain for 31.7 nm (a), 23.2 nm (b), 17.5 nm (c), 11.7 nm (d) and 3.1 nm (e). Fig. 5 (a-e) are meant only to visually depict the density and distribution of the ½<111>-type dislocations. It can be inferred that as the grain sizes decrease, the density of dislocations decreases too. Dislocations themselves act as obstructions to the movement of other dislocations. Interaction of dislocations causes work-hardening, the degree of which depends on the distance between the active slip planes. The work-hardening is higher if the distance between the active slip planes is small. If multiple dislocations intersect at a dislocation junction, the formation of dislocation jogs takes place that act as hard obstacles and

pin the dislocation, thereby causing rapid hardening [57]. Thus, higher the density of intersecting dislocations, higher work hardening is achieved and higher the flow stress. To validate our predictions, we compute densities of ½<111>-type dislocations for all grain sizes at the strain where the flow stress is obtained, as mentioned above. The densities of dislocations with Burgers vector ½<111> type are presented as function of grain size in Fig. 4(f). Only ½<111>-type dislocations have been considered because these are the dominant dislocation type in a BCC lattice with the smallest repeat vector. The linear relationship between flow stress and the square root of the dislocation density fitted using least-squares is consistent with previously established results [58].

GBs serve as stronger obstacles than line or point defects to dislocation motion and impede the transmittance of dislocations into adjacent grains. Macroscopic yielding is realized only when at least 5 slip systems are activated in each grain of the material [57]. But microscopic yielding can occur in some grains that are favorably aligned relative to the applied stress. Therefore, dislocations within such grains pile up against the GBs and are not transmitted to the adjacent grain, as it happens to be the Hall-Petch regime. Hence, we see a large dislocation pile up in Figs. 5(a) and (b) when grain sizes are ≥ 23.2 nm, *i.e.,* the critical size. When the grain sizes are further reduced, the GB volume fraction increases and they serve as defect sinks [59], decreasing the dislocation densities as observed from Figs. 5(c) and (d). When the grain size is 3.1 nm there is practically little or no dislocation generation, and the deformation effectively occurs due to GB sliding (Fig 5 (e)).

4. Conclusions

We conclude that, at the crossover from Hall-Petch to inverse Hall-Petch, the critical grain size produces a maximum flow stress due to a maximum density of ½<111> dislocations (4.47×10^{12} cm^{-2}) that intersect each other and pile up at the GBs. Below the critical grain size, the GB migration and slipping phenomena are activated that reduce the flow stress, and the effect is pronounced on further reducing the grain sizes. The dislocations being unable to pile up at GBs, the latter do not impart strengthening to the alloy below the critical grain size. We note that the critical grain size in alloys and MPEAs is larger than those in pure metals like cubic iron and Au. This larger grain size arises because the disorder at the GBs and the grain junctions [47] thicken

faster as the grain sizes reduce in alloys as compared to metals, related to the fact that GBs and grain junctions are disordered and presence of multiple species promotes the disorder in the GB more than when only single species is present. Thus, GBs thickens at a relatively larger grain size in alloys as compared to pure metals and the transition to inverse Hall-Petch phenomenon happens at a larger grain size in alloys. This behavior is also evinced from prior works where iron was found to have a critical grain size of 14.1 nm [31] and nanocrystalline gold was found to have the inverse Hall-Petch effect in 5-10 nm range [60] while the transition happened at 18.9 nm for BCC $CoNiFeAl_{0.7}Cu_{0.3}$ [33].

In summary, we employ classical MD simulations to perform unidirectional tensile deformation of nanocrystalline $(Mo_{0.95}W_{0.05})_{0.85}Ta_{0.10}(TiZr)_{0.05}$ MPEA with mean grain sizes ranging from 3.1 to 31.7 nm, and to examine them for a transition to inverse Hall-Petch behavior. The phase and microstructural evolution recorded from these samples reveal that the alloy assumes a BCC phase consistent with prior literature [30], with some distribution of amorphous phase due to the presence of GBs. The amorphous phase increases progressively as the grain sizes are reduced because the volume fraction of GBs increases by ~60% with lowering grain sizes. The stress-strain profile resulting from the tensile deformation reveals that flow stress increases as the grain size is reduced from 31.7 nm to 23.2 nm, but decreases thereafter with further diminishing of the grain size. The maximum flow stress of 9.76 GPa occurs for samples with 23.2 nm grains. The microstructural characterization corroborates that when the grain size ≥ 23.2 nm (critical grain size), deformation is driven by dislocation gliding and stress induced phase transformation from BCC to FCC phases. However, the deformation mechanism shifts to GB migration and sliding below the critical grain size. The transition from Hall-Petch to inverse Hall-Petch behavior is attributed to the maximization of the dislocation density (4.47×10^{12} cm^{-2}) and dislocation pile up at the GB. This finding is supported by the observed Taylor-like behavior [61], that is, linear variation of the flow stress with the square root of the dislocation density.

Acknowledgements

The work was supported by the U.S. Department of Energy (DOE), Office of Energy Efficiency and Renewable Energy, Advanced Manufacturing Office (AMO) under design project WBS

2.1.0.19 led by Ames Laboratory, which is operated by Iowa State University for the U.S. DOE under contract DE-AC02-07CH11358.

References:

[1] J.W. Yeh, S.K. Chen, S.J. Lin, J.Y. Gan, T.S. Chin, T.T. Shun, C.H. Tsau, S.Y. Chang, Nanostructured high-entropy alloys with multiple principal elements: novel alloy design concepts and outcomes, Advanced Engineering Materials, 6 (2004) 299-303.
[2] B. Cantor, I.T.H. Chang, P. Knight, A.J.B. Vincent, Microstructural development in equiatomic multicomponent alloys, Mat Sci Eng a-Struct, 375 (2004) 213-218.
[3] E.P. George, W. Curtin, C.C. Tasan, High entropy alloys: A focused review of mechanical properties and deformation mechanisms, Acta Materialia, 188 (2020) 435-474.
[4] B.S. Murty, J.-W. Yeh, S. Ranganathan, P. Bhattacharjee, High-entropy alloys, Elsevier, 2019.
[5] E.P. George, D. Raabe, R.O. Ritchie, High-entropy alloys, Nature Reviews Materials, 4 (2019) 515-534.
[6] M. Gianelle, A. Kundu, K. Anderson, A. Roy, G. Balasubramanian, H.M. Chan, A novel ceramic derived processing route for Multi-Principal Element Alloys, Materials Science and Engineering: A, 793 (2020) 139892.
[7] A. Roy, G. Balasubramanian, Predictive descriptors in machine learning and data-enabled explorations of high-entropy alloys, Computational Materials Science, (2021) 110381.
[8] H. Khakurel, M. Taufique, A. Roy, G. Balasubramanian, G. Ouyang, J. Cui, D.D. Johnson, R. Devanathan, Machine learning assisted prediction of the Young's modulus of compositionally complex alloys, Scientific reports, 11 (2021) 1-10.
[9] X. Yang, Y. Zhang, Prediction of high-entropy stabilized solid-solution in multi-component alloys, Materials Chemistry and Physics, 132 (2012) 233-238.
[10] C. Li, J. Li, M. Zhao, Q. Jiang, Effect of alloying elements on microstructure and properties of multiprincipal elements high-entropy alloys, Journal of Alloys and Compounds, 475 (2009) 752-757.
[11] K. Zhang, S. Pan, W. Tang, Y. Zhang, B. Wei, Structural and bonding transformation of Al0. 67CrCoCuFeNi high-entropy alloys during quenching, Journal of Alloys and Compounds, 753 (2018) 636-641.
[12] J.M. Rickman, H.M. Chan, M.P. Harmer, J.A. Smeltzer, C.J. Marvel, A. Roy, G. Balasubramanian, Materials informatics for the screening of multi-principal elements and high-entropy alloys, Nat Commun, 10 (2019) 2618.
[13] A. Roy, T. Babuska, B. Krick, G. Balasubramanian, Machine learned feature identification for predicting phase and Young's modulus of low-, medium-and high-entropy alloys, Scripta Materialia, 185 (2020) 152-158.
[14] P. Singh, A. Sharma, A.V. Smirnov, M.S. Diallo, P.K. Ray, G. Balasubramanian, D.D. Johnson, Design of high-strength refractory complex solid-solution alloys, npj Computational Materials, 4 (2018) 1-8.
[15] P. Singh, S. Gupta, S. Thimmaiah, B. Thoeny, P.K. Ray, A.V. Smirnov, D.D. Johnson, M.J. Kramer, Vacancy-mediated complex phase selection in high entropy alloys, Acta Materialia, 194 (2020) 540-546.
[16] P. Singh, A.V. Smirnov, A. Alam, D.D. Johnson, First-principles prediction of incipient order in arbitrary high-entropy alloys: exemplified in Ti0. 25CrFeNiAlx, Acta Materialia, 189 (2020) 248-254.
[17] P. Singh, A.V. Smirnov, D.D. Johnson, Atomic short-range order and incipient long-range order in high-entropy alloys, Physical Review B, 91 (2015) 224204.
[18] P. Singh, A.V. Smirnov, D.D. Johnson, Ta-Nb-Mo-W refractory high-entropy alloys: anomalous ordering behavior and its intriguing electronic origin, Physical Review Materials, 2 (2018) 055004.

[19] F. Otto, A. Dlouhý, C. Somsen, H. Bei, G. Eggeler, E.P. George, The influences of temperature and microstructure on the tensile properties of a CoCrFeMnNi high-entropy alloy, Acta Materialia, 61 (2013) 5743-5755.
[20] C. Varvenne, A. Luque, W.A. Curtin, Theory of strengthening in fcc high entropy alloys, Acta Materialia, 118 (2016) 164-176.
[21] A. Roy, P. Sreeramagiri, T. Babuska, B. Krick, P.K. Ray, G. Balasubramanian, Lattice distortion as an estimator of solid solution strengthening in high-entropy alloys, Materials Characterization, (2021) 110877.
[22] A. Roy, J. Munshi, G. Balasubramanian, Low energy atomic traps sluggardize the diffusion in compositionally complex refractory alloys, Intermetallics, 131 (2021) 107106.
[23] E. Hall, The deformation and ageing of mild steel: III discussion of results, Proceedings of the Physical Society. Section B, 64 (1951) 747.
[24] N. Petch, The cleavage strength of polycrystals, Journal of the Iron and Steel Institute, 174 (1953) 25-28.
[25] A.H. Cottrell, Theory of brittle fracture in steel and similar metals, Trans. Met. Soc. AIME, 212 (1958).
[26] A. Chokshi, A. Rosen, J. Karch, H. Gleiter, On the validity of the Hall-Petch relationship in nanocrystalline materials, Scripta metallurgica, 23 (1989) 1679-1684.
[27] J. Schiøtz, F.D. Di Tolla, K.W. Jacobsen, Softening of nanocrystalline metals at very small grain sizes, Nature, 391 (1998) 561-563.
[28] S. Yip, The strongest size, Nature, 391 (1998) 532-533.
[29] A. Sharma, G. Balasubramanian, Dislocation dynamics in Al0.1CoCrFeNi high-entropy alloy under tensile loading, Intermetallics, 91 (2017) 31-34.
[30] P. Singh, A. Sharma, A.V. Smirnov, M.S. Diallo, P.K. Ray, G. Balasubramanian, D.D. Johnson, Design of high-strength refractory complex solid-solution alloys, npj Computational Materials, 4 (2018) 16.
[31] J.B. Jeon, B.-J. Lee, Y.W. Chang, Molecular dynamics simulation study of the effect of grain size on the deformation behavior of nanocrystalline body-centered cubic iron, Scripta Materialia, 64 (2011) 494-497.
[32] M.R. Jones, B.L. Nation, J.A. Wellington-Johnson, J.F. Curry, A.B. Kustas, P. Lu, M. Chandross, N. Argibay, evidence of inverse Hall-petch Behavior and Low friction and Wear in High entropy Alloys, Scientific Reports, 10 (2020) 1-8.
[33] S. Chen, Z.H. Aitken, Z. Wu, Z. Yu, R. Banerjee, Y.-W. Zhang, Hall-Petch and inverse Hall-Petch relations in high-entropy CoNiFeAlxCu1-x alloys, Materials Science and Engineering: A, 773 (2020) 138873.
[34] S. Plimpton, Fast parallel algorithms for short-range molecular dynamics, Sandia National Labs., Albuquerque, NM (United States), 1993.
[35] A. Stukowski, Visualization and analysis of atomistic simulation data with OVITO–the Open Visualization Tool, Modelling and Simulation in Materials Science and Engineering, 18 (2009) 015012.
[36] P. Hirel, Atomsk: a tool for manipulating and converting atomic data files, Computer Physics Communications, 197 (2015) 212-219.
[37] Z. Pan, Y. Li, Q. Wei, Tensile properties of nanocrystalline tantalum from molecular dynamics simulations, Acta Materialia, 56 (2008) 3470-3480.
[38] X. Zhou, R. Johnson, H. Wadley, Misfit-energy-increasing dislocations in vapor-deposited CoFe/NiFe multilayers, Physical Review B, 69 (2004) 144113.
[39] A. Sharma, P. Singh, D.D. Johnson, P.K. Liaw, G. Balasubramanian, Atomistic clustering-ordering and high-strain deformation of an Al 0.1 CrCoFeNi high-entropy alloy, Scientific reports, 6 (2016) 31028.
[40] P. Sreeramagiri, A. Roy, G. Balasubramanian, Effect of Cooling Rate on the Phase Formation of AlCoCrFeNi High-Entropy Alloy, Journal of Phase Equilibria and Diffusion, (2021) 1-9.

[41] A.V. Shapeev, Moment tensor potentials: A class of systematically improvable interatomic potentials, Multiscale Modeling & Simulation, 14 (2016) 1153-1173.
[42] A. Ferrari, B. Dutta, K. Gubaev, Y. Ikeda, P. Srinivasan, B. Grabowski, F. Körmann, Frontiers in atomistic simulations of high entropy alloys, Journal of Applied Physics, 128 (2020) 150901.
[43] J. Li, Q. Fang, B. Liu, Y. Liu, Y. Liu, Mechanical behaviors of AlCrFeCuNi high-entropy alloys under uniaxial tension via molecular dynamics simulation, RSC advances, 6 (2016) 76409-76419.
[44] Y.-H. Wen, Z.-Z. Zhu, R.-Z. Zhu, Molecular dynamics study of the mechanical behavior of nickel nanowire: Strain rate effects, Computational Materials Science, 41 (2008) 553-560.
[45] D. Faken, H. Jónsson, Systematic analysis of local atomic structure combined with 3D computer graphics, Comput. Mater. Sci, 2 (1994) 279-286.
[46] J. Schiøtz, K.W. Jacobsen, A maximum in the strength of nanocrystalline copper, Science, 301 (2003) 1357-1359.
[47] P. Keblinski, S. Phillpot, D. Wolf, H. Gleiter, Amorphous structure of grain boundaries and grain junctions in nanocrystalline silicon by molecular-dynamics simulation, Acta materialia, 45 (1997) 987-998.
[48] H. Song, B. Duan, Y. Wang, M. An, Y. Li, Enhanced plasticity by introducing amorphous phase in nanopolycrystal Cu: A molecular dynamics study, Materials Chemistry and Physics, 253 (2020) 123254.
[49] F. Zhao, J. Zhang, C. He, Y. Zhang, X. Gao, L. Xie, Molecular dynamics simulation on creep behavior of nanocrystalline tial alloy, Nanomaterials, 10 (2020) 1693.
[50] A.R. Hinkle, J.F. Curry, H. Lim, B.L. Nation, M.R. Jones, J. Wellington-Johnson, P. Lu, N. Argibay, M. Chandross, Low friction in BCC metals via grain boundary sliding, Physical Review Materials, 4 (2020) 063602.
[51] Y. Zhang, S. Jiang, M. Wang, Atomistic investigation on superelasticity of NiTi shape memory alloy with complex microstructures based on molecular dynamics simulation, International Journal of Plasticity, 125 (2020) 27-51.
[52] R.K. Rajgarhia, D.E. Spearot, A. Saxena, Plastic deformation of nanocrystalline copper-antimony alloys, Journal of Materials Research, 25 (2010) 411-421.
[53] V. Yamakov, D. Wolf, S. Phillpot, A. Mukherjee, H. Gleiter, Deformation mechanism crossover and mechanical behaviour in nanocrystalline materials, Philosophical magazine letters, 83 (2003) 385-393.
[54] V. Pozdnyakov, A. Glezer, Structural mechanisms of plastic deformation in nanocrystalline materials, Physics of the Solid State, 44 (2002) 732-737.
[55] F. Louchet, J. Weiss, T. Richeton, Hall-Petch law revisited in terms of collective dislocation dynamics, Physical Review Letters, 97 (2006) 075504.
[56] W. Wei, L. Liu, H. Gong, M. Song, M. Chang, D. Chen, Fundamental mechanism of BCC-FCC phase transition from a constructed PdCu potential through molecular dynamics simulation, Computational Materials Science, 159 (2019) 440-447.
[57] T.H. Courtney, Mechanical behavior of materials, Waveland Press, 2005.
[58] H. Conrad, S. Feuerstein, L. Rice, Effects of grain size on the dislocation density and flow stress of niobium, Materials Science and Engineering, 2 (1967) 157-168.
[59] H. Gleiter, Grain boundaries as point defect sources or sinks—diffusional creep, Acta Metallurgica, 27 (1979) 187-192.
[60] J. Liu, X. Fan, W. Zheng, D.J. Singh, Y. Shi, Nanocrystalline gold with small size: inverse Hall–Petch between mixed regime and super-soft regime, Philosophical Magazine, 100 (2020) 2335-2351.
[61] G.I. Taylor, The mechanism of plastic deformation of crystals. Part I.—Theoretical, Proceedings of the Royal Society of London. Series A, Containing Papers of a Mathematical and Physical Character, 145 (1934) 362-387.

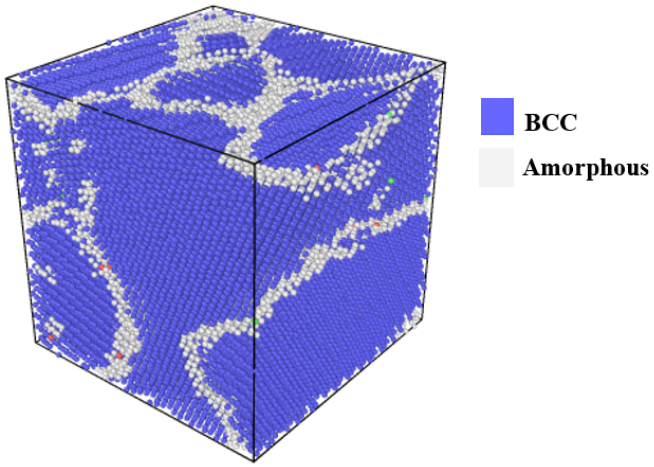

Figure 1: Local structural coordination revealed through CNA in equiatomic MoTaTiWZr. The alloy crystallizes into majority BCC phase, which validates the accuracy of the potential adopted in this work. The GB region is amorphous as there is a lack of long-range order in the GB regions.

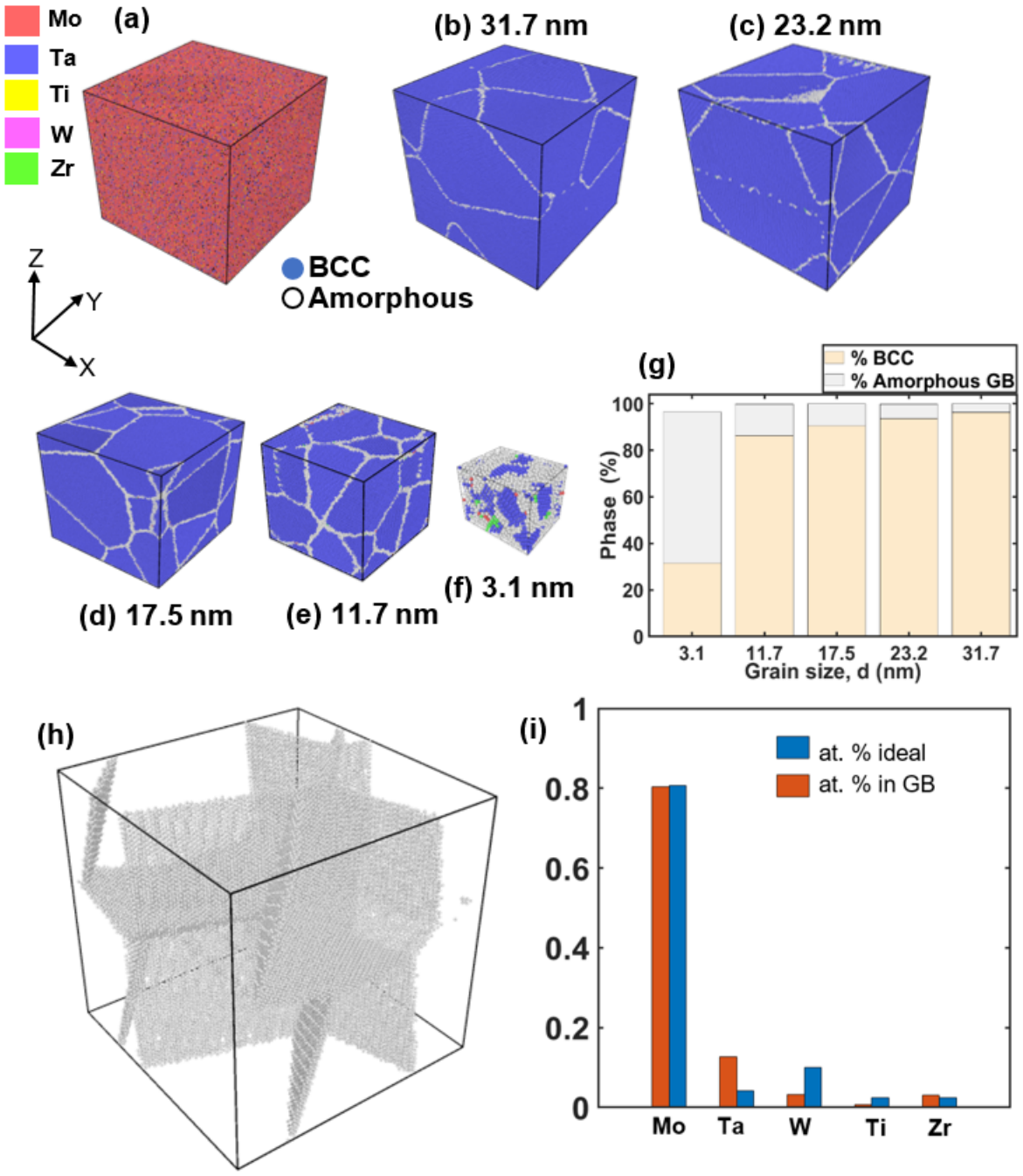

Figure 2: (a) Representation of $(Mo_{0.95}W_{0.05})_{0.85}Ta_{0.10}(TiZr)_{0.05}$ in a polycrystalline simulation cell where color legend denotes atom types. Figures **(b-f)** represent the crystallographic phases for different samples as determined from structural coordination using common neighbor analysis (CNA) on the equilibrated cells. Sample (b) with 31.7-nm-sized grains is constructed by

accommodating 2 grains in a simulation box with 40 nm edge, while the sample (c) with grains of size 23.2 nm is created by accommodating 5 grains in a similar simulation box. Thus, the simulation-cell samples (b) and (c) have equal edge length but different number of grains. Below 23.2 nm, the edge dimension of the cuboidal cells decrease as the number of grains in each of those simulation boxes is maintained to be the same to demonstrate the reducing grain size. CNA reveals the MPEA is primarily a single-phase BCC with some amorphous phase due to presence of GBs. **(g)** Phase fraction as a function of grain size shows decrease in the crystalline volume fraction with the decrease in grain size because of larger fraction of the alloy is occupied by the amorphous GBs. **(h)** Representation of the non-structured atoms that from the GBs: only those atoms that comprise the GB have been filtered out for a qualitative examination. **(i)** Distribution of elements by % atomic fraction in the GBs evinces presence of excess Ta and dearth of W in the GB regions as compared to the ideal atomic percent.

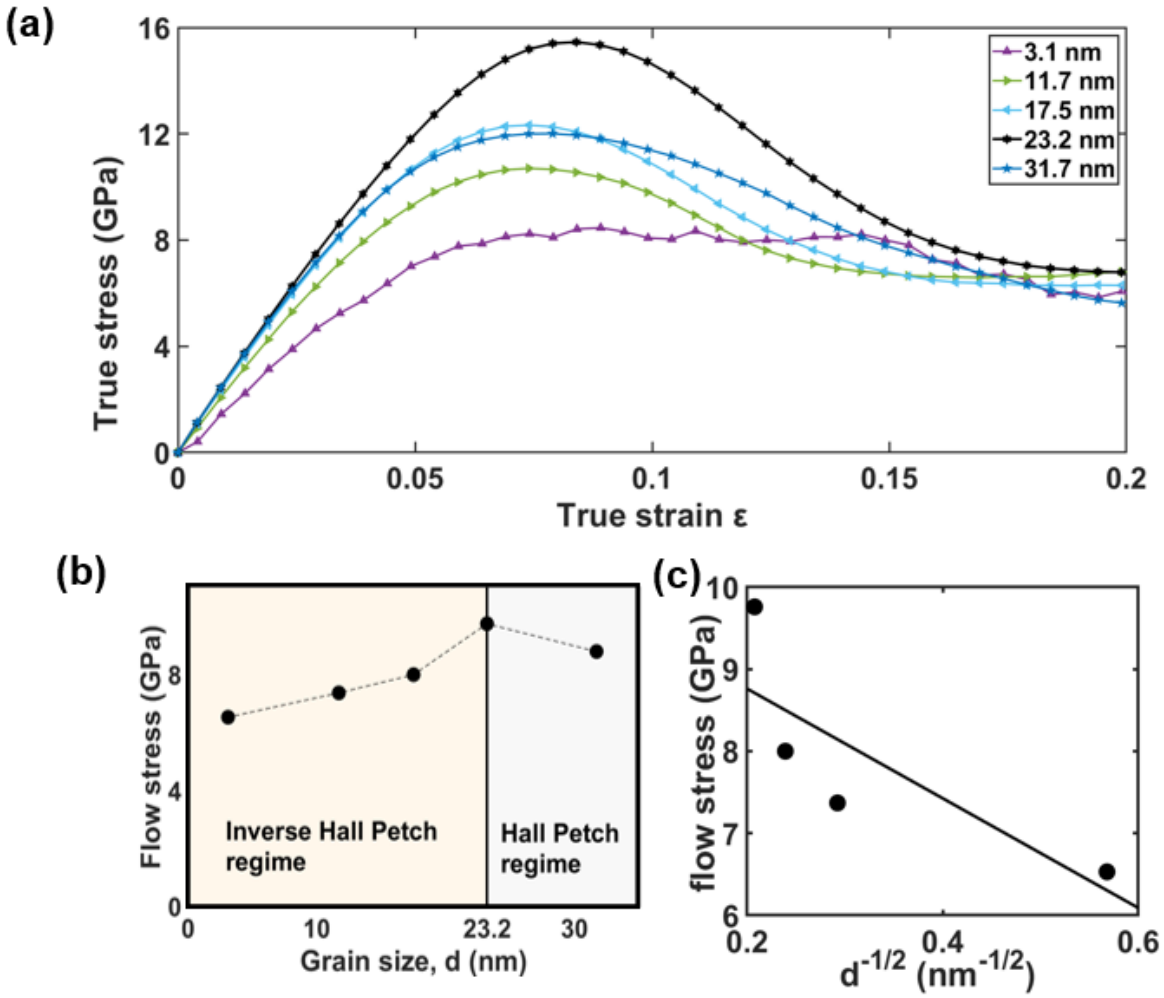

Figure 3: (a) Grain-size effects on the stress-strain curve during uniaxial strain in the loading direction (σ_{xx}) for each grain size due to mechanical deformation. In the linear region, the deformation curve is elastic. However, in the plastic region, initiation of dislocations with Burgers vector **b**=<111>/2 causes stress drops to occur and curves level off subsequently. The critical grain size for transition from Hall-Petch to inverse Hall-Petch is predicted to be 23.2 nm at which the maximum flow stress is exhibited. **(b)** The average flow stress transition from Hall-Petch to inverse Hall-Petch (decreasing as grain size is reduced) is distinctly observed. **(c)** The flow stress is presented as a function of grain size in the inverse Hall-Petch region. The inverse Hall-Petch relation is $\sigma_{flow} = 10.097–6.678\times d^{-1/2}$, where the negative slope indicates the inverse effect.

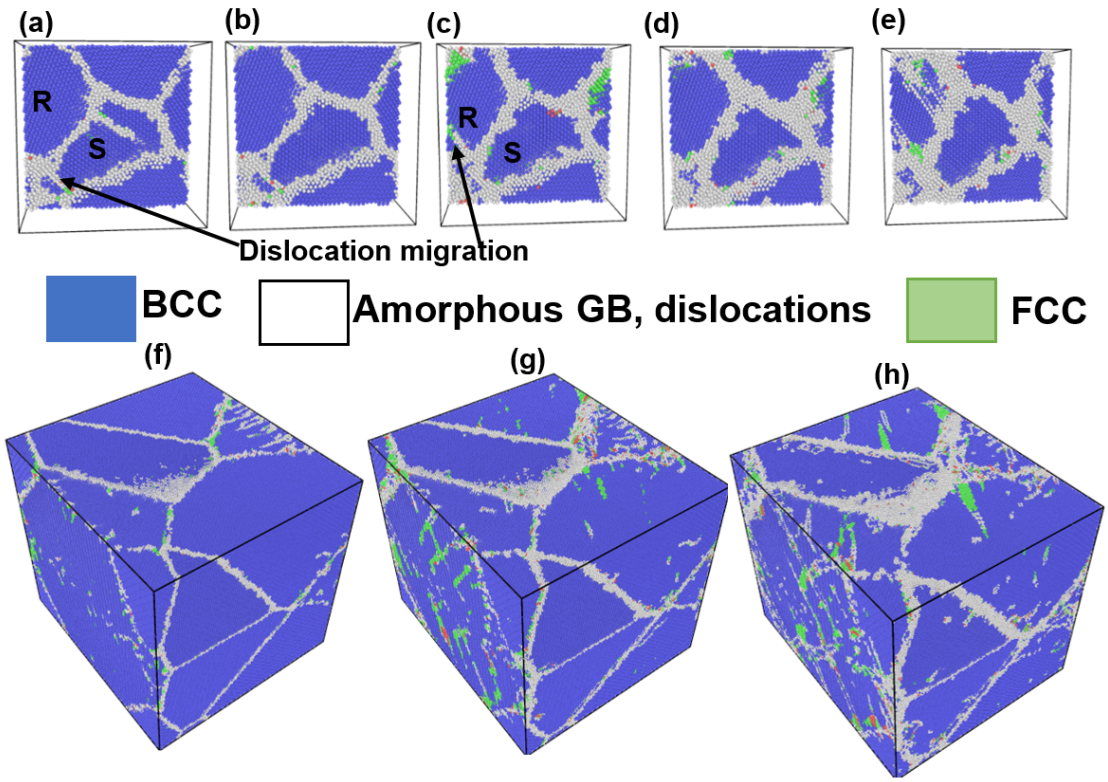

Figure 4: Snapshots of GB and bulk atoms with their local structural coordination. GB migration under unidirectional tension in the simulation cell with 3.1 nm grains results in considerable thickening of GB at (a) 1%, (b) 3%, (c) 5%, (d) 7% and (e) 9% strain. Grain R shown in (a) undergoes significant reorientation from (a) to (e) indicating a grain rotation has occurred with respect to the GB. Dislocation migration is observed from grain S (a) into grain R (c) via the GB separating the two. Thickening of GB implies bulk flow and sliding of GB atoms within the GB volume. Minor traces of phase transformation to FCC in (c) and (e) are observed suggesting that the deformation occurs due to a coupled effect of GB migration and phase transformation. (f), (g) and (h) display the deformation of 40 nm simulation cell with 5 grains under uniaxial tension at 1%, 3% and 5% strain, respectively during which the FCC phase fraction increases from 1.2 % to 4.3 %. Here, the local phase transformation from BCC to FCC distinctly appears as the major deformation mechanism consistent with deformation mechanism of other BCC MPEAs [33].

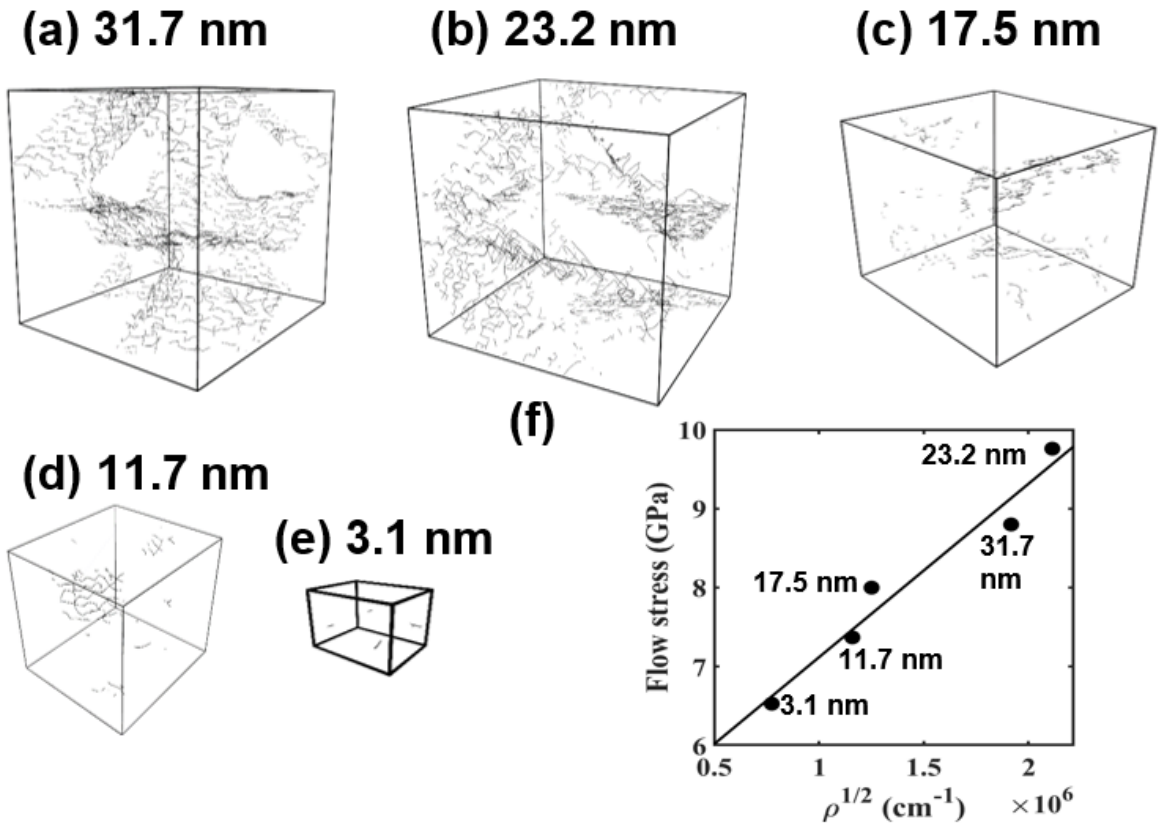

Figure 5: ½<111>-type dislocation evolution in $(Mo_{0.95}W_{0.05})_{0.85}Ta_{0.10}(TiZr)_{0.05}$ represented by simulation cells with grain sizes: (a) 31.7 nm (b) 23.2 nm (c) 17.5 nm (d) 11.7 nm (e) 3.1 nm at 5.0 % strain. (f) Average flow stress as a function of the dislocation density for all grain sizes reveals an somewhat linear trend with R^2 = 0.96, consistent with prior findings [52]. At the inflection point (23.2 nm) from Hall-Petch to inverse Hall-Petch behavior, a maximum flow stress is noted at the critical grain size due to the occurrence of the highest density of ½<111> dislocations (4.47×10^{12} cm^{-2}) that are intersecting and pile up at the GBs.